

# Visible light driven hydrogen evolution by molecular nickel catalysts with time-resolved spectroscopic and DFT insights

Ho, Xian Liang; Shao, Haiyan; Ng, Yik Yie; Ganguly, Rakesh; Lu, Yunpeng; Soo, Han Sen

2019

Ho, X. L., Shao, H., Ng, Y. Y., Ganguly, R., Lu, Y., & Soo, H. S. (2019). Visible light driven hydrogen evolution by molecular nickel catalysts with time-resolved spectroscopic and DFT insights. *Inorganic Chemistry*, 58(2), 1469-1480. doi:10.1021/acs.inorgchem.8b03003

<https://hdl.handle.net/10356/103691>

<https://doi.org/10.1021/acs.inorgchem.8b03003>

---

This document is the Accepted Manuscript version of a Published Work that appeared in final form in *Inorganic Chemistry*, copyright © American Chemical Society after peer review and technical editing by the publisher. To access the final edited and published work see <https://doi.org/10.1021/acs.inorgchem.8b03003>.

*Downloaded on 20 Mar 2024 18:44:26 SGT*

# Visible Light Driven Hydrogen Evolution by Molecular Nickel Catalysts with Time-Resolved Spectroscopic and DFT Insights

*Xian Liang Ho,<sup>a,b</sup> Haiyan Shao,<sup>a,b</sup> Yik Yie Ng,<sup>a</sup> Rakesh Ganguly,<sup>a</sup> Yunpeng Lu,<sup>a</sup> and Han Sen*

*Soo<sup>\*a,b</sup>*

<sup>a</sup> Division of Chemistry and Biological Chemistry, School of Physical and Mathematical Sciences, Nanyang Technological University, Singapore 637371.

<sup>b</sup> Solar Fuels Laboratory, Nanyang Technological University, 50 Nanyang Avenue, Singapore 639798.

**KEYWORDS** Visible light photocatalysis; hydrogen evolution reaction; nanosecond time-resolved optical spectroscopy; DFT calculations; mechanistic studies; solar energy conversion

## Abstract

Hydrogen ( $H_2$ ) is a clean fuel that can potentially be a future solution for the storage of intermittent renewable energy. However, current  $H_2$  production is mainly dominated by the energy intensive steam reforming reaction, which consumes a fossil fuel, methane, and emits copious amounts of carbon dioxide as one of the byproducts. To address this challenge, we report a molecular catalyst that produces  $H_2$  from aqueous solutions, is composed of affordable, earth-abundant elements such as nickel, and has been incorporated into a system driven by visible light. Under optimized conditions, we observe a turnover number of 3880, among the best for photocatalytic  $H_2$  evolution with nickel complexes from water-methanol solutions. Through nanosecond transient absorption, electron paramagnetic resonance, and UV-visible spectroscopic measurements, and supported by density functional theory calculations, we report a detailed study of this photocatalytic  $H_2$  evolution cycle. We demonstrate that a one-electron reduced, predominantly ligand-centered, reactive Ni intermediate can be accessed under visible light irradiation using triethylamine as the sacrificial electron donor and reductive quencher of the initial photosensitizer excited state. In addition, the computational calculations suggest that the second coordination sphere ether arms can enhance the catalytic activity by promoting proton relay, similar to the mechanism among [FeFe] hydrogenases in Nature. Our study can form the basis for future development of  $H_2$  evolution molecular catalysts that incorporate both ligand redox noninnocence *and* alternative second coordination sphere effects in artificial photosynthetic systems driven by visible light.

## Introduction

With the growing threat of global climate change, intensified efforts have been devoted to the development of sustainable energy sources to reduce the reliance on fossil fuels.<sup>1</sup> The storage of solar energy in chemical bonds, also known as artificial photosynthesis, by splitting  $H_2O$  into  $H_2$

(proton reduction) and  $\text{O}_2$  ( $\text{H}_2\text{O}$  oxidation), has been explored as a potentially clean and carbon-free solution.<sup>2</sup> Semiconductor materials such as metal chalcogenides and phosphides have emerged as cost-effective replacements for the unsurpassed platinum (Pt) as the photo- or electrocatalyst for proton reduction to  $\text{H}_2$ .<sup>3</sup> Nonetheless, although such heterogeneous systems exhibit remarkably high  $\text{H}_2$  production rates or even self-healing abilities, detailed mechanistic investigations of the interfacial chemical processes remain challenging. In contrast, molecular photocatalytic systems are often highly selective and active, more amenable to spectroscopic probes for the elementary reaction steps, and can be systematically designed and improved through ligand variations. Typically, molecular photocatalytic  $\text{H}_2$  evolution systems consist of a light absorbing photosensitizer and a proton reduction catalyst, each of which can be independently optimized.<sup>4</sup> Thus, some critical aspects of creating improved artificial photosynthetic systems include the development of an affordable, efficient  $\text{H}_2$  evolution catalyst, and a thorough understanding of the light absorption and electron transfer events.<sup>5</sup>

Historically, integrated photocatalytic systems comprising platinum-group metals (PGMs) like Pt,<sup>6</sup> Rh,<sup>7</sup> Ir,<sup>8</sup> and Pd<sup>9</sup> have exhibited respectable performance for light absorption and  $\text{H}_2$  evolution by the same molecule. However, new catalysts consisting of earth-abundant, first-row transition metals are increasingly sought after as more sustainable alternatives, due to the high price of PGMs.<sup>10</sup> For instance, cobalt-containing cobaloxime catalysts have been combined with a multitude of photosensitizers to produce  $\text{H}_2$ , although they have demonstrated modest stability and turnover numbers (TON) thus far.<sup>11</sup> Cobalt polypyridyl complexes have also shown competent  $\text{H}_2$  production activity under photodriven conditions.<sup>12</sup> On the other hand, although DuBois, Bullock, and coworkers have reported nickel (Ni)  $\text{P}_2\text{N}_2$  complexes with exceptional *electrocatalytic*  $\text{H}_2$  evolution activity exceeding that of even enzymatic systems,<sup>13</sup> the Ni  $\text{P}_2\text{N}_2$  compounds exhibited

surprisingly low turnover frequencies (TOF)<sup>14</sup> for *photocatalytic* proton reduction until the second coordination sphere has been modified with phosphonic acid groups and the catalyst has been immobilized on metal oxide semiconductors.<sup>15</sup> In addition, Eisenberg and coworkers have presented seminal studies on homogeneous catalysis with redox noninnocent ligands by using Co dithiolene<sup>16</sup> and Ni thiolates<sup>17</sup> for the photogeneration of H<sub>2</sub> from aqueous organic solutions. Notably, their recent Ni pyridinethiolate molecular catalyst and photosensitizer system displayed an outstanding TON of 7300 in 30 h, with a proposed mechanism similar to the proton relays in natural hydrogenase enzymes.<sup>17b</sup> Several other non-amine proton relays in small molecule redox catalysis have also been explored by Nocera and coworkers.<sup>18</sup> They reported that incorporating different proton relays on the second coordination sphere of metal complexes enhanced the H<sub>2</sub> evolution reaction (HER) and lowered the overpotential compared to the unmodified catalyst. These studies collectively demonstrated the importance of proton relays in the second coordination spheres of transition metal-based catalysts for efficient catalytic HER.

As part of an effort toward artificial photosynthetic systems,<sup>19</sup> our group has embarked on a research program to explore and optimize the light absorption,<sup>20</sup> charge separation,<sup>21</sup> and multielectron catalytic<sup>22</sup> functions. We had previously synthesized and employed new Ni salicylaldimine catalysts with pendant ether arms in the second coordination sphere to bind hydrated alkali metal cations and provide hydrogen-bonding stabilization for enhanced electrocatalytic H<sub>2</sub> evolution reactivity.<sup>22a</sup> Polyether appended salicylaldimine complexes have lately been explored by Yang, Blakemore, and others and shown to be effective for chelating alkali metal cations to form bimetallic complexes.<sup>23</sup> The coordinated and hydrated alkali metal cations can in turn act as non-amine proton relays to enhance HER by steering water molecules in close proximity to the metal center.<sup>22a</sup> This approach capitalized on established principles in

supramolecular chemistry that crown ethers effectively chelate alkali metal cations and Lewis acids will increase the Bronsted acidity of coordinated water molecules, thus resulting in enhanced activity especially for proton-dependent catalysis.<sup>24</sup> In addition, the unbound ether groups can also form hydrogen-bonding interactions with water, which will raise the local concentration of water near the catalytically active metal center to promote the multi-electron and multi-proton transfer processes in HER.

We have now developed a more robust and active Ni salicylaldimine catalyst in *only two steps* from affordable, commercially available reagents that can be incorporated into a molecular photocatalytic H<sub>2</sub> evolution system. This new Ni complex includes peripheral ether arms as well to allow us to investigate the effects of balancing ligand redox noninnocence and second coordination sphere effects on the H<sub>2</sub> evolution catalysis. Under optimized conditions, we utilized Ir<sup>III</sup>(ppy)<sub>2</sub>(dtbbpy) (ppy = 2-phenylpyridine; dtbbpy = 4,4'-di-*tert*-butyl-2,2'-bipyridine, [Ir]) as a light-harvester and triethylamine (TEA) as a sacrificial electron donor and reductive quencher to achieve a photocatalytic H<sub>2</sub> evolution TON of 3880 within 6 h under visible light irradiation (> 420 nm), with H<sub>2</sub>O and methanol as the proton sources. Motivated by these results, we performed detailed experiments to elucidate the elementary steps of the H<sub>2</sub> evolution catalytic cycle through nanosecond transient absorption, electron paramagnetic resonance (EPR), and UV-visible spectroscopic measurements, further supported by intermediate isolation studies and density functional theory (DFT) calculations. This study provides the mechanistic insights for small molecule activation and second coordination sphere effects in homogeneous catalysis, which can aid in the systematic improvement of HER activity not only for molecular systems,<sup>10b, 25</sup> but also for heterogeneous catalysts.

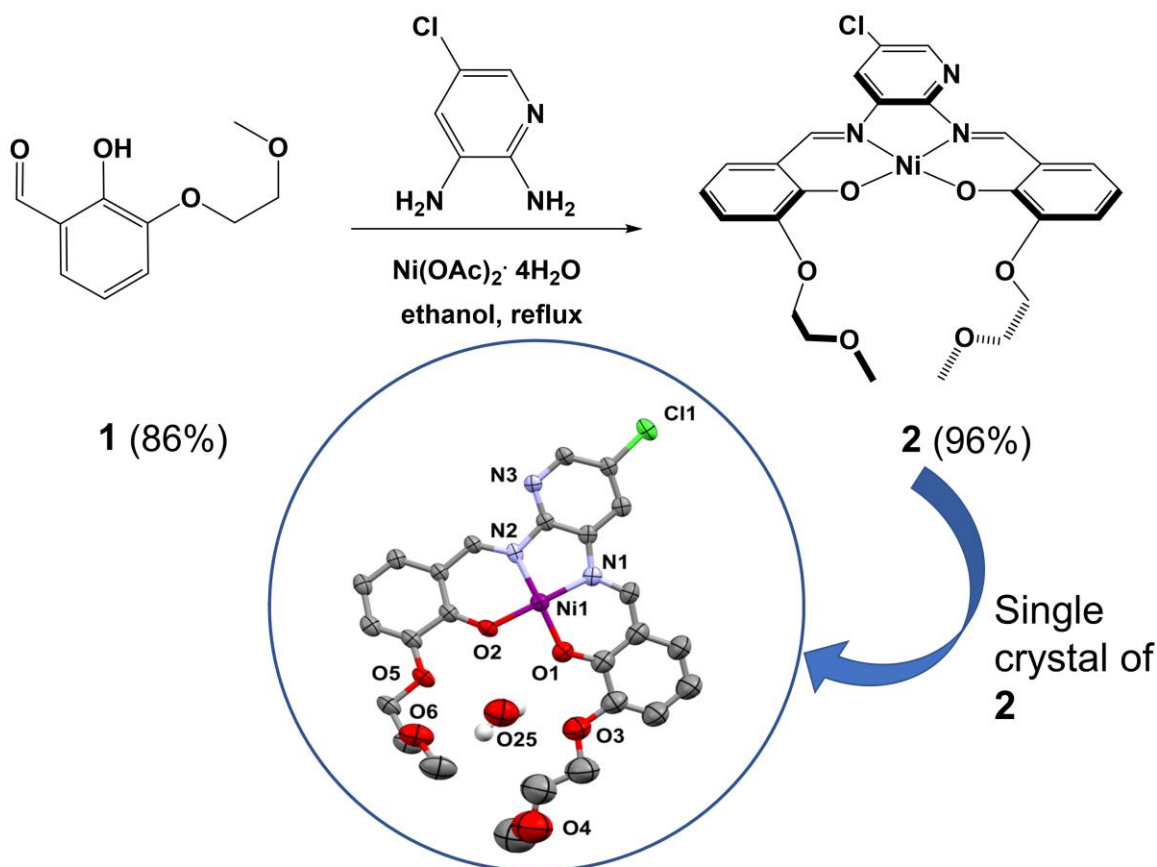
## Results and Discussion

### Synthesis and characterization of nickel complex

The nickel complex **2** was synthesized in high yields (83%) over *only two steps* from affordable, commercially available reagents (Scheme 1). In the first step, 2,3-dihydroxybenzaldehyde was modified with a 2-methoxyethoxy ether arm to give 2-hydroxy-3-(2-methoxyethoxy)benzaldehyde (**1**). Subsequently, **1** reacted with 2,3-diamino-5-chloropyridine *via* a condensation reaction in the presence of nickel acetate in methanol (MeOH) to yield complex **2** as a deep red powder. Complex **2** was fully characterized by nuclear magnetic resonance (NMR) spectroscopy, high-resolution mass spectrometry (HRMS), elemental analyses, and UV-visible spectroscopy. The UV-visible spectrum of **2** (Figure S1, Supporting Information, SI) in the Supporting Information (SI) exhibits two absorbance peaks at 380 and 488 nm in MeOH (containing 5% H<sub>2</sub>O) with extinction coefficients of 18700 and 4820 M<sup>-1</sup>cm<sup>-1</sup>, which can respectively be assigned to charge transfers arising from  $\pi$ - $\pi^*$  transitions of the salicyaldimine ligand and a local excitation from the HOMO with spin density on the nickel and phenoxy motifs to the LUMO that is largely localized on the pyridine (Figure S2, SI).

Single crystals of **2** were obtained by slow evaporation from a DCM solution, after which the molecular structure was determined by X-ray crystallography (Scheme 1). The coordination geometry of **2** is similar to the Ni complex in our previous report,<sup>22a</sup> with a square planar geometry around Ni, corresponding to a  $d^8$  electronic configuration. Notably, a H<sub>2</sub>O molecule is trapped in the pendant ether arm of the secondary coordination sphere. The ether arm could thus potentially direct H<sub>2</sub>O molecules and protons toward the Ni center during the catalytic cycle, assisting in the evolution of H<sub>2</sub>. Other details of the crystallographic data can be found in Tables S1-6 (SI).

**Scheme 1. Synthetic Steps and X-ray Crystal Structure<sup>a</sup> for Nickel Complex 2.**



<sup>a</sup> Solvents and hydrogen atoms except the ones in H<sub>2</sub>O are omitted for clarity.

The cyclic voltammogram of **2** (Figure 1a) in acetonitrile (ACN) saturated with argon shows three redox waves. The quasi-reversible redox wave ( $E_{1/2}$ ) at 0.30 V vs. Fc<sup>+</sup>/Fc can be assigned to the **2**<sup>+</sup>/**2** redox couple, whereas the irreversible reduction wave at -1.87 V can be attributed to the **2**/**2**<sup>-</sup> redox couple (Figure 1b).<sup>26</sup> This access to multiple redox states implies that we may be able to employ **2** as a redox catalyst, especially for the H<sub>2</sub> evolution reaction. The irreversibility of the redox wave at -1.87 V, even at different scan rates, is likely due to an electron transfer followed by a chemical reaction (i.e. an EC process) where two ligand radicals dimerize under electrochemical conditions.<sup>26</sup> This dimerization is a possible deactivation pathway<sup>27</sup> that can

explain the absence of electrocatalytic H<sub>2</sub> evolution by **2**, despite the fact that it is active under dilute, photocatalytic conditions (*vide infra*).

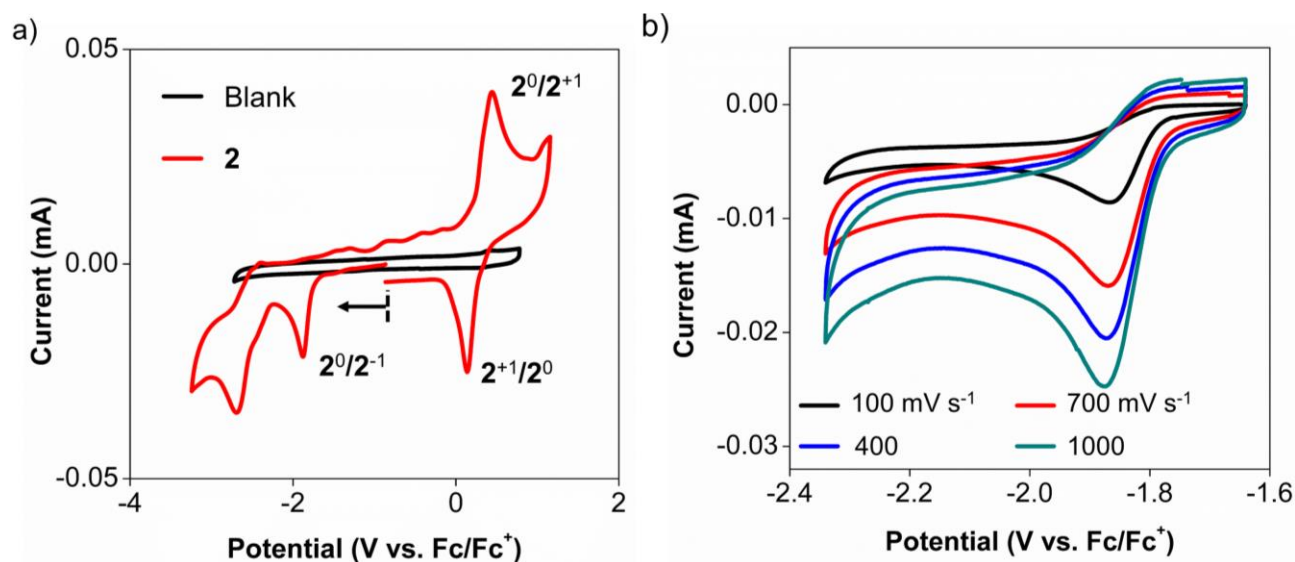


**Figure 1.** a) CV of 0.10 M *n*-Bu<sub>4</sub>NPF<sub>6</sub> in ACN with a glassy carbon electrode (3 mm diameter) in the absence (black) and presence of 1.0 mM **2** (red) at a scan rate of 100 mV s<sup>-1</sup>. b) CV of the solution of 1.0 mM **2** in part a) with increasing scan rates from 100 to 1000 mV s<sup>-1</sup> in the potential window of -1.63 to -2.35 V (vs Fc<sup>+</sup>/Fc).

A series of photodriven H<sub>2</sub> evolution experiments were thus performed using a solution of **2** as the catalyst. Compound [Ir] was chosen as the photosensitizer due to its long excited state lifetime, established photophysical characteristics, and highly reducing potential of -1.91 V vs Fc<sup>+</sup>/Fc.<sup>28</sup> These known properties will allow us to focus on investigating the role of **2** in the photocatalytic system. TEA was used as the sacrificial electron donor under *visible light* irradiation with 5% water in methanol as the solvent to solubilize all the components. During each catalytic experiment, the amount of H<sub>2</sub> built up in the headspace was quantified by gas chromatography (GC, Table S7, SI) and calculated by subtracting the H<sub>2</sub> produced from the control experiments that were conducted in the absence of **2**.

The H<sub>2</sub> produced *versus* time profiles with different catalyst concentrations ranging from 1.0 to 10.0  $\mu$ M are displayed in Figure 2a. For every experiment, we subtracted the amount of H<sub>2</sub> produced by [Ir] only (Figure S3, SI) from the total amount of H<sub>2</sub> measured. Although the amount of H<sub>2</sub> that was produced increased as the concentration of **2** rose, the highest TON of 3880 was achieved with only 2.0  $\mu$ M of **2** (red line, Figure 2b). At even lower catalyst loadings when 1.0  $\mu$ M of **2** was used, the TON was comparable to the ones with 2.0  $\mu$ M of **2** only for the first 2 h of irradiation. However, the H<sub>2</sub> evolution activity for 1.0  $\mu$ M of **2** decreased dramatically after the initial 2 h and the TON finally reached a value in between the experiments with 5.0  $\mu$ M and 10.0  $\mu$ M of **2** after 6 h, probably due to the inactivation of **2** (*vide infra*). Our experiments indicated that at concentrations of **2** above 2  $\mu$ M, the H<sub>2</sub> evolution performance per unit catalyst was lower, which may be caused by the formation of binuclear or polynuclear salicylaldimine complexes in the solution.<sup>29</sup> To support this, we observed the presence of an intermediate with a *m/z* ratio of 1112.57 when we conducted liquid chromatography-mass spectrometry (LCMS) measurements on the one-electron reduced **2**<sup>-</sup> (*vide infra*) at high concentrations (Figure S4, SI), which is consistent with a binuclear complex with a calculated *m/z* of 1112.13. The LCMS also displayed the presence of **2**<sup>-</sup> with a *m/z* of 556.25 (expected *m/z* of 556.62) and a product that is likely to be [**2**<sup>-</sup> + ligand] with the loss of one Ni center at a *m/z* ratio of 1056.92 (expected *m/z* of 1056.22). This suggested that the loss of Ni may be a pathway for the deactivation of **2** to form catalytically inoperative intermediates containing **2**<sup>-</sup> bound to a demetallated ligand. However, it is also possible that the loss of Ni by **2**<sup>-</sup> occurs only during the LCMS experiment, so we cannot definitively conclude that demetallation of **2** or **2**<sup>-</sup> is the major catalyst deactivation pathway.

A control experiment with 2.0  $\mu$ M of **2** conducted in anhydrous methanol under otherwise identical conditions (entry 5, Table S1, SI) revealed that the TON was almost halved to 1900, suggesting

that H<sub>2</sub>O was a more effective proton source, albeit not the only one in this photocatalytic system. An attempt to use Ru(bpy)<sub>3</sub>(PF<sub>6</sub>)<sub>2</sub> ([Ru]) as the light harvester led to a low TON of only 52 (Entry 13, Table S7, SI), suggesting that a sufficiently reducing photosensitizer was required for optimal activity. Photosensitizers composed of only earth-abundant elements such as Cu and organic variants including Eosin Y and Eosin B were also evaluated, but the amount of H<sub>2</sub> produced was below the detection limits of our GC (Entries 17-20, Table 7, SI). Catalyst **2** was also more active than our previously reported Ni salicylaldimine complex,<sup>22a</sup> which led to a TON of 2800 under the same photocatalytic conditions at 2.0  $\mu$ M of the catalyst (Entry 15, Table S7, SI).

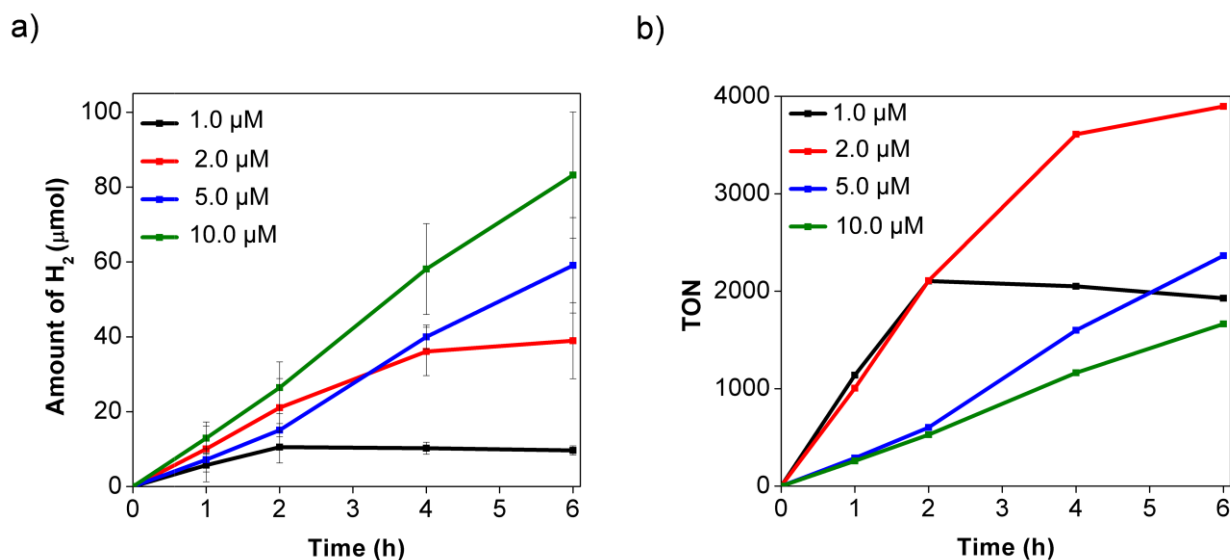


**Figure 2.** The (a) amount in  $\mu$ mol, and (b) TON of H<sub>2</sub> produced with [**2**] = 1.0  $\mu$ M (black), 2.0  $\mu$ M (red), 5.0  $\mu$ M (blue), and 10  $\mu$ M (green) in a methanol (5% H<sub>2</sub>O) solution containing 0.10 mM of [Ir] and 0.10 M TEA under 6 h of visible light irradiation. The amounts of H<sub>2</sub> generated for each data point were obtained as an average of at least three independent measurements.

We observed that the rate of H<sub>2</sub> production slowed down drastically after 6 h of visible light irradiation in all the experiments. Furthermore, this decrease in the rate of H<sub>2</sub> production was

accelerated at lower concentrations of **2** (Figure S5, SI), prompting us to perform additional experiments to identify the cause. Since TEA was added in large excess, we ruled it out as the limiting reagent, and examined if the other components were responsible for this deactivation after 6 h. Using the optimized conditions with 2.0  $\mu\text{M}$  of **2**, when 0.10 mM of fresh [Ir] was added to the photocatalytic reaction after 6 h, the  $\text{H}_2$  evolution did not resume. This indicated that photosensitizer deactivation was not the main reason that  $\text{H}_2$  evolution slowed down. On the other hand, the addition of one extra equivalent of **2** led to an 80% recovery of  $\text{H}_2$  production in the following 6 h (Figure S6, SI). Control experiments were also carried out in the absence of **2**, [Ir], TEA, or light, which verified that the amount of  $\text{H}_2$  produced was reduced dramatically (Table S7, SI). These results establish that all the components are essential for efficient  $\text{H}_2$  gas production, and the deactivation of **2** is the main cause for the reduction in  $\text{H}_2$  evolution reactivity.

Furthermore, to investigate if the  $\text{H}_2$  was produced from  $\text{H}_2\text{O}$ /methanol or from TEA, the reaction was conducted using  $\text{D}_2\text{O}$  and deuterated methanol ( $\text{MeOD}$ ) with unlabeled TEA. Helium gas was employed as the carrier gas to distinguish between  $\text{H}_2$  and  $\text{D}_2$ .<sup>30</sup> By comparing with the GC data of  $\text{H}_2$  and  $\text{D}_2$  standard gases, we observed a signal which confirmed that majority of the product formed was likely to be  $\text{D}_2$ , with  $\text{H}_2$  below our detection limits (Figure S7, SI). On the other hand, we mainly detected  $\text{H}_2$  when undeuterated solvents and TEA were used. Therefore, we propose that  $\text{H}_2\text{O}$ , which undergoes rapid proton exchange with methanol, is probably the proton donor instead of TEA.

The  $\text{H}_2$  evolution rate was also affected by the nominal pH of the solution as shown in Figure S8, SI. Since the solvent system is a methanolic solution with small amounts of added water, the pH of the buffered solutions will not be identical to the expected values in aqueous solutions. Thus, we experimentally verified the value in each reaction solution by using a pH meter. We observed

that H<sub>2</sub> evolution started to increase only from around a pH of 8.4 and became optimal at a pH around 10.0. When the pH of the solution was raised to 11, H<sub>2</sub> evolution ceased. We propose that at pH values below 8.4, the TEA would be protonated, which would prevent its critical function as the reductive quencher of the initial photoexcited [Ir]\* to form the reduced [Ir]<sup>-</sup> necessary for the catalytic cycle to operate. Above a pH of 10.0, the decline in proton concentrations would start to affect protonation of the Ni catalyst, leading to the dramatic decrease in the rate of H<sub>2</sub> evolution. This optimal pH window for H<sub>2</sub> evolution under photocatalytic conditions with a sacrificial electron donor and reductive quencher were also previously observed in studies when the well-known cobaloxime (Co<sup>III</sup>(dmgH)<sub>2</sub>pyCl) was employed as a H<sub>2</sub> evolution catalyst.<sup>31</sup> Finally, to determine whether **2** was a precatalyst in a homogeneous or heterogeneous system since recent work<sup>32</sup> has shown that zero-valent nickel nanoparticles are capable of photocatalytic H<sub>2</sub> evolution as well, dynamic light scattering (DLS) experiments were carried out on the reaction mixture after 6 h of irradiation. No nanoparticles were observed in the reaction mixture (Figure S9, SI), suggesting that **2** operated in a homogeneous molecular catalytic cycle.

With the optimized catalytic conditions in hand, we sought a deeper understanding of the reaction pathway in the catalytic cycle through time-resolved spectroscopic experiments. There are two generally accepted pathways for the single photon absorption followed by electron transfer in molecular photosensitizer reactions. In one route, the photosensitizer absorbs light, after which its excited state is reduced by a sacrificial electron donor. The reduced photosensitizer is then recovered by transferring an electron to the catalyst enroute to producing H<sub>2</sub>. Alternatively, the photosensitizer absorbs light, forms a transient excited state species, and transfers an electron to the catalyst directly. The oxidized photosensitizer is then reduced to its original oxidation state by the sacrificial electron donor. To gain some insights into the elementary reaction steps during the

photocatalysis, nanosecond transient absorption spectroscopic (TAS) and transient emission spectroscopic (TES) experiments were conducted with 355 nm pulsed irradiation of 0.10 mM [Ir] in methanol containing 5% H<sub>2</sub>O. The samples were probed by a broadband xenon lamp beam before and after 5 – 8 ns pulses. In all our TAS data, the detected intensity of the transmitted signals is presented as the logarithm of the ratio ( $\Delta OD$ ) of the light intensity from the probe beam *after* laser excitation to the intensity *before* laser excitation. The  $\Delta OD$  thus refers to increased absorption (positive  $\Delta OD$ ) or reduced absorption/emission (negative  $\Delta OD$ ) of the transient photoexcited species relative to the ground state.

At 570 nm near the emission maximum of [Ir], the photoluminescence lifetime of [Ir]\* is  $390 \pm 20$  ns, which we define as  $\tau_0$  (Figure S10a, SI). We subsequently monitored the quenching effect of each component in the catalytic system on the [Ir]\* lifetime (Figure S10b-d, SI) in the presence of different concentrations of TEA and **2**. The Stern-Volmer plots (Figure S11, SI) were obtained after fitting the photoluminescence decay lifetimes of the signal at 570 nm to a single exponential, yielding a quenching rate constant,  $k_q$ , of  $5.66 \times 10^6 \text{ M}^{-1} \text{ s}^{-1}$  in the presence of TEA. Interestingly, **2** does not quench the photoexcited [Ir] (Table S8, SI), suggesting that [Ir]\* is likely to be reductively quenched by TEA to form [Ir]<sup>-</sup> first, after which [Ir]<sup>-</sup> then transfers an electron to reduce **2** to **2**<sup>-</sup>.

TAS experiments were then conducted on solutions of [Ir] alone (Figure 3a) and with TEA, in the absence and presence of **2**, as depicted in Figures 3b and 3c, respectively. The spectra were recorded at  $\mu\text{s}$  time-scales to monitor the long-lived intermediates during and after charge transfer processes have taken place. The transient absorption spectra in the absence of **2** shows the decay of the characteristic absorption maxima at 380 and 485 nm and the emission maximum at 590 nm of [Ir]\*, concomitant with the formation of a new species with absorptions at 385, 448, 498, and

530 nm that does not decay within 90  $\mu$ s (Figure 3b). The spectral signatures at 385, 498, and 530 nm confirmed the formation of  $[\text{Ir}]^-$  through reductive quenching by TEA.<sup>7b</sup> In the presence of **2** (Figure 3c), the formation of  $[\text{Ir}]^-$  *via* reductive quenching by TEA was also observed from the spectral signature at 530 nm. However, the absorption bands at 385 and 498 decayed within 4  $\mu$ s (Figure S12, SI, decay of 530 nm band obscured by growing intermediate) and a new intermediate, likely **2**<sup>-</sup>, with a broad absorption spectral feature from 580 to 700 nm was formed (Figure 3d). In addition, the kinetics of the absorption at 380 and 630 nm were explored. At and above 630 nm, the  $\Delta\text{OD}$  for the formation of  $[\text{Ir}]^-$  is zero so it will have no contribution to the TAS. Thus, the two lifetimes obtained at this wavelength from the fits to the decay kinetics will then correspond to the decay of  $[\text{Ir}]^*$  and the formation of **2**<sup>-</sup>. At 380 nm, the longest time component corresponds to the decay of  $[\text{Ir}]^-$  (Figure S13, SI). By comparing the longest time components at 380 and 630 nm, we find that the formation of **2** (Figure S13, SI) is concurrent with the decay of  $[\text{Ir}]^-$ , verifying the correlation between the two different processes. The shorter lifetimes obtained from absorption at 380 nm can be attributed to the decay processes of  $[\text{Ir}]^*$ . Based on these TAS experiments, we propose that the proton reduction catalytic cycle is initiated by the reductive quenching of  $[\text{Ir}]$  by TEA after photoexcitation, followed by electron transfer from  $[\text{Ir}]^-$  to **2**.

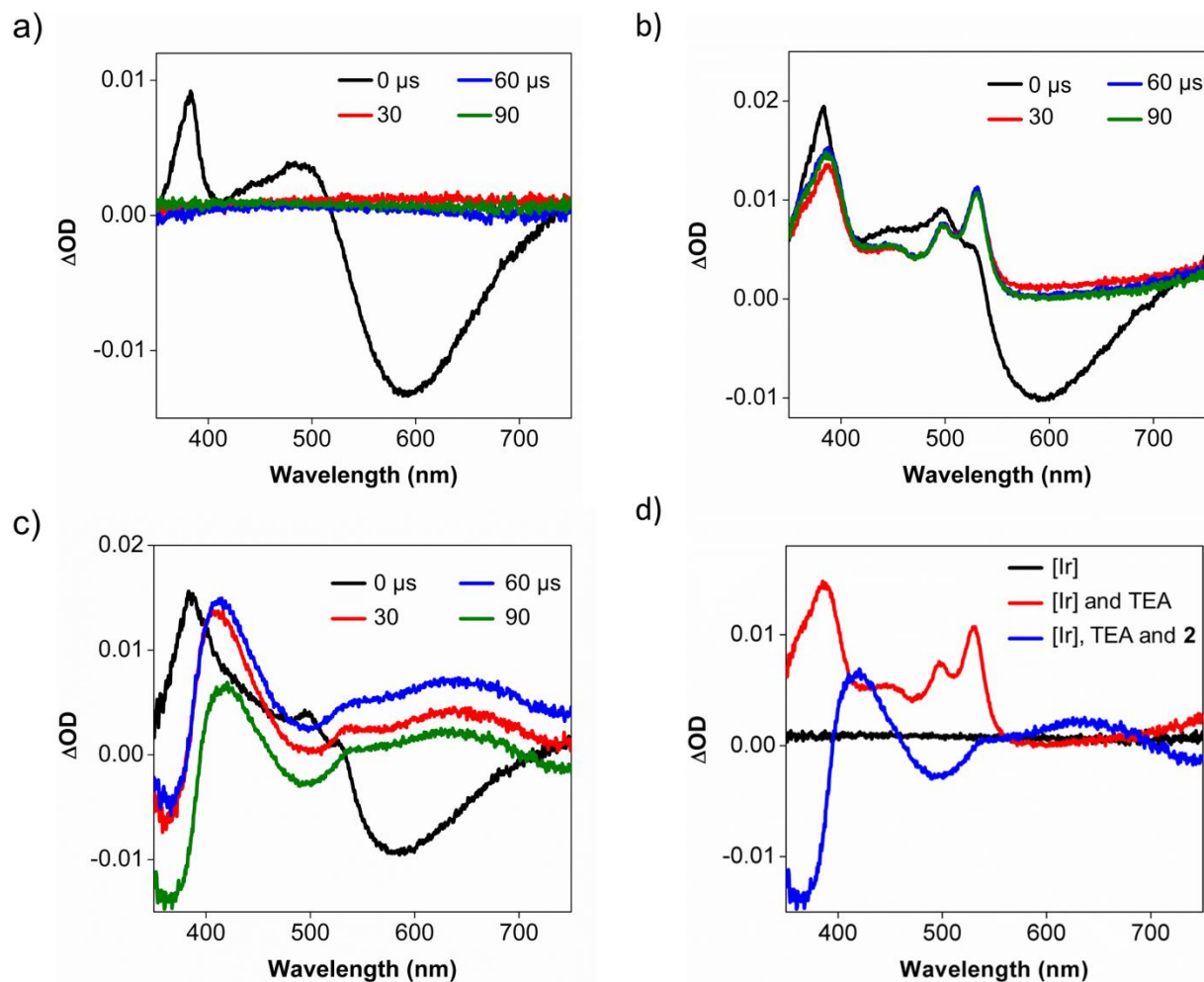


**Figure 3.** Transient absorption spectra upon 355 nm pulsed irradiation of (a) 0.10 mM of [Ir], (b) 0.10 mM of [Ir] with 0.10 M of TEA, and (c) 0.10 mM of [Ir] with 0.10 M of TEA and 40  $\mu$ M of **2**. (d) A comparison of the spectra at 90  $\mu$ s of the three samples with different compositions. In parts (a) – (c), the 0  $\mu$ s spectra correspond to the changes right after illumination, within the time resolution of the spectrometer.

To verify that **2** can be reduced by  $[\text{Ir}]^-$  during the  $\text{H}_2$  evolution cycle, we attempted to independently synthesize some of the possible intermediates of **2** during catalysis. We added one equivalent of magnesium anthracene as a one-electron chemical reductant<sup>33</sup> under anhydrous

conditions at room temperature to **2**, and characterized the one-electron reduced product, **2**<sup>-</sup>, by NMR, EPR and steady-state UV-visible spectroscopy. Further reduction is not expected since magnesium anthracene does not have sufficient potential to effect the second reduction of **2**. The <sup>1</sup>H NMR spectrum of the crude reaction mixture containing **2**<sup>-</sup> did not exhibit any signals from **2** itself or dissociated ligand, although anthracene was detected (Figure S14a SI). Even when the experiment was performed with a broader chemical shift range between -10 to 190 ppm, paramagnetically shifted or broadened signals were not observed (Figure S14b, SI), suggesting that **2**<sup>-</sup> is probably paramagnetic.

To complement this data, solid-state EPR spectroscopic measurements were performed to determine if the unpaired electron on **2**<sup>-</sup> was metal- or ligand-centered. The EPR spectrum exhibits axial symmetry with  $g_{\parallel} = 2.0678$  and  $g_{\perp} = 2.0081$  with no hyperfine splitting at room temperature (Figure 4a), indicating that **2**<sup>-</sup> likely contains an organic radical with the unpaired electron residing predominantly on the ligand, since these features are inconsistent with typical Ni(I) complexes that have  $g$  values of 2.12 to 2.15 and much larger anisotropies.<sup>34</sup> These  $g$  values also match those from structurally similar complexes such as [Ni(saloph)]<sup>-</sup> (saloph = *N,N'*-disalicylidene-*o*-phenylenediaminate), which was reported to arise from a ligand-centered reduction.<sup>34</sup> The EPR spectrum of sodium anthracenide only, as depicted in Figure 4b, displays an isotropic signal with  $g = 2.0023$  as expected. Although we cannot fully rule out the presence of small amounts of anthracenide radical anion in the EPR sample for **2**<sup>-</sup>, we had thoroughly rinsed the sample and do not anticipate much remaining. Furthermore, given the high sensitivity of EPR spectroscopy, we believe that the EPR signals in Figure 4a can be mostly attributed to the radical anion localized on the ligand, though we cannot completely exclude the presence of some Ni-centered spin density due to the covalency of the Ni-ligand interactions. We were not able to structurally characterize **2**<sup>-</sup>

despite multiple attempts to recrystallize it and thus, we cannot definitively conclude that  $\mathbf{2}^-$  is a mononuclear Ni complex. However, we believe that the evidence based on the kinetics of  $\mathbf{2}^-$  for  $\text{H}_2$  evolution catalysis, the converged structure of  $\mathbf{2}^-$  in the DFT calculations below, and the EPR spectra are not consistent with a dimer formed from radical coupling of two ligands each supporting  $\text{Ni}^{\text{II}}$ , which should be diamagnetic.

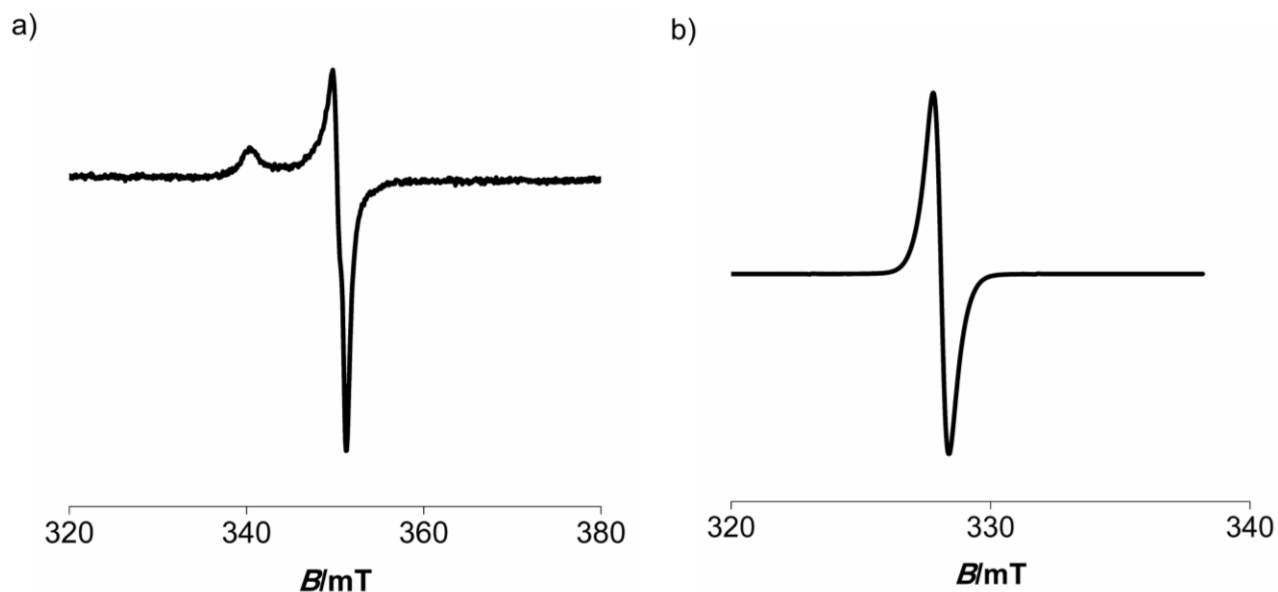


**Figure 4.** EPR spectra of (a)  $\mathbf{2}^-$  collected with a microwave frequency of 9850 Mhz and (b) sodium anthracenide collected with a microwave frequency of 9200 MHz.

DFT calculations with geometry optimization in MeOH as the solvent were also performed by using the M06 functional. Notably, the singly occupied molecular orbital (SOMO) of  $\mathbf{2}^-$  appeared to be predominantly localized on the ligand (Figure S2b, SI). A natural population analysis on  $\mathbf{2}^-$  also demonstrated that the spin density population is almost zero on the Ni center, concurring with our proposal above that the unpaired electron after reduction was predominantly delocalized on

the ligand. Overall, both the experimental and computational data support a ligand-centered reduction of **2**. This is consistent with recent results that demonstrate the importance of redox non-innocent ligands in facilitating charge transfer during H<sub>2</sub> evolution reactions.<sup>10b, 35</sup>

With the **2**<sup>-</sup> accessed by chemical reduction in hand, we sought to compare and match its photophysical properties with those from the time-resolved measurements. Based on the TAS data at 90 μs, a long-lived intermediate had formed in the reaction mixture containing [Ir], TEA, and **2** (blue line, Figure 3d). In addition, the steady-state UV-visible spectra of **2** and **2**<sup>-</sup> are illustrated in Figure 5a. By using the steady-state spectra of **2**<sup>-</sup> (red line, Figure 5a) and **2** (black line, Figure 5a), we can obtain the difference spectrum (red line, Figure 5b) and compare it with the TAS data at 90 μs, reproduced again from Figure 3d (black line). Interestingly, we observe spectral absorption signatures at 413 nm, 540 nm, and 580-700 nm for the steady-state data, similar to the 90 μs spectrum from the TAS measurements, as displayed in Figure 5b. In addition, we conducted HER experiments with **2**<sup>-</sup> and observed that the catalysis was first order (Figure S15, SI) with respect to its concentration. The TON obtained with 2 μM of **2**<sup>-</sup> after 6 h (entry 14, Table S7, SI) was also similar to the TON for the HER reactions with **2**, which suggested that **2**<sup>-</sup> was indeed an active intermediate in the catalytic cycle. Consequently, we believe that the optical spectroscopic and kinetic measurements concur with a model where [Ir]\* is reductively quenched by TEA, which in turn then reduces **2** to **2**<sup>-</sup> in the first step of the photocatalytic H<sub>2</sub> evolution cycle.

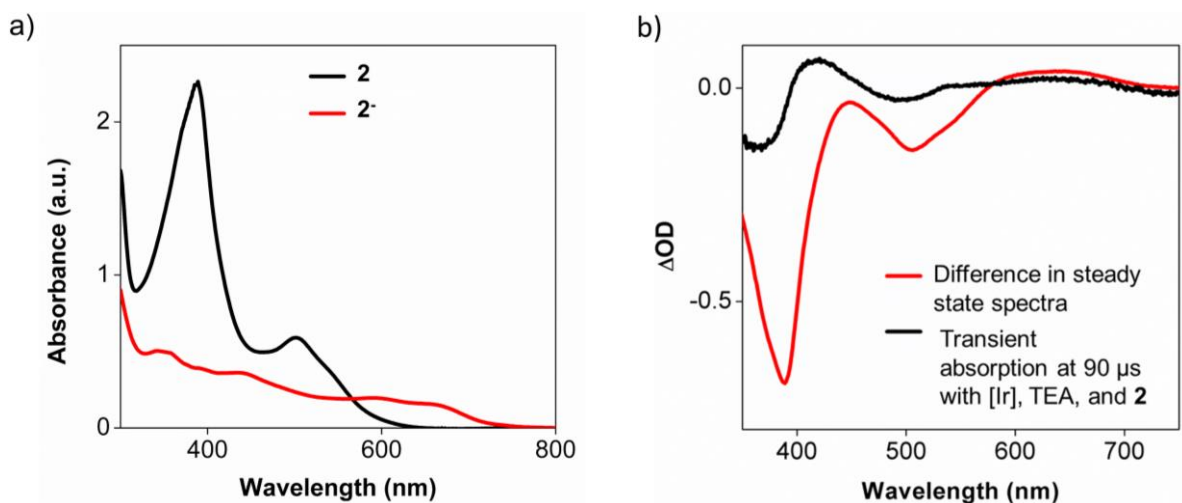


**Figure 5.** (a) The steady-state absorption spectra of **2** (black) and **2<sup>-</sup>** (red) in tetrahydrofuran (THF). (b) Difference in steady-state spectra by subtracting **2** from **2<sup>-</sup>** (red) in comparison to the TAS data at 90 μs of the mixture containing [Ir], TEA, and **2** (black), the latter of which has been reproduced from Figure 2d.

In order to explore the effects of removing hydrogen bonding interactions with H<sub>2</sub>O while still preventing the oligomerization that is notorious among Ni salicylaldimine complexes, the ether arms were replaced with *tert*-butyl groups to give **3** (Scheme 2). Complex **3** was then evaluated as a H<sub>2</sub> evolution catalyst under the same optimized conditions as above with [Ir], TEA, and methanol with 5% H<sub>2</sub>O under visible light irradiation. Remarkably, no H<sub>2</sub> was detected by GC, underscoring the essential function of the second coordination sphere ether arm in **2** (entry 16, Table S7, SI). The CVs in THF illustrate a cathodic shift of the first reduction potential in **3** at -2.07 V, as compared to a potential of -1.85 V in **2** (Figure 6). Thus, both the cathodically shifted redox potential and the lack of ether groups to hydrogen bond with H<sub>2</sub>O molecules may contribute to the catalytic inactivity of **3**.

**Scheme 2. Synthetic Steps for the *Tert*-Butyl Substituted **3**.**

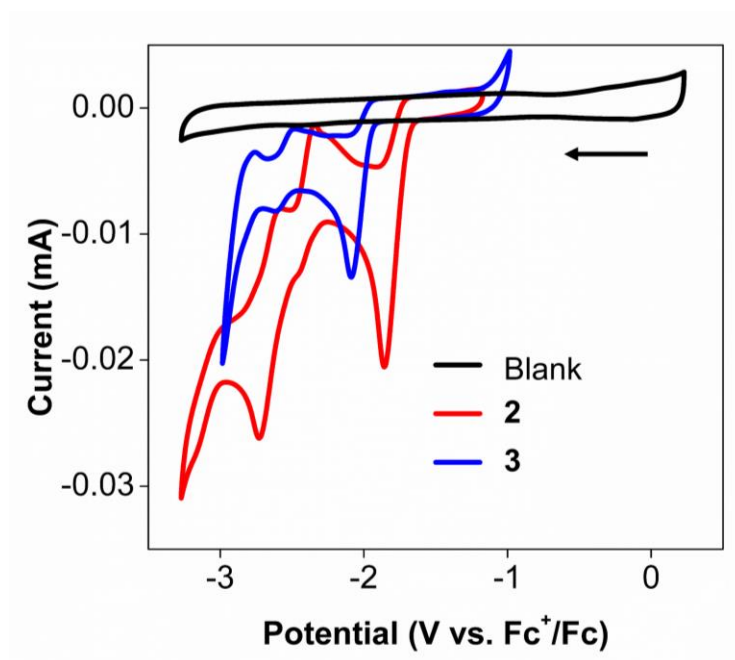
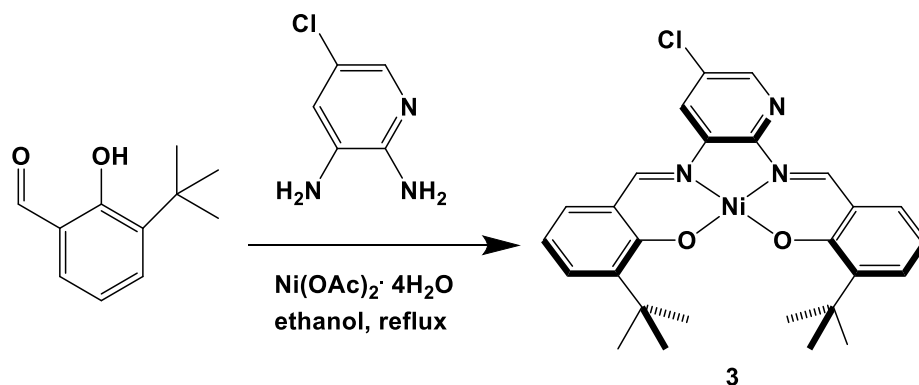


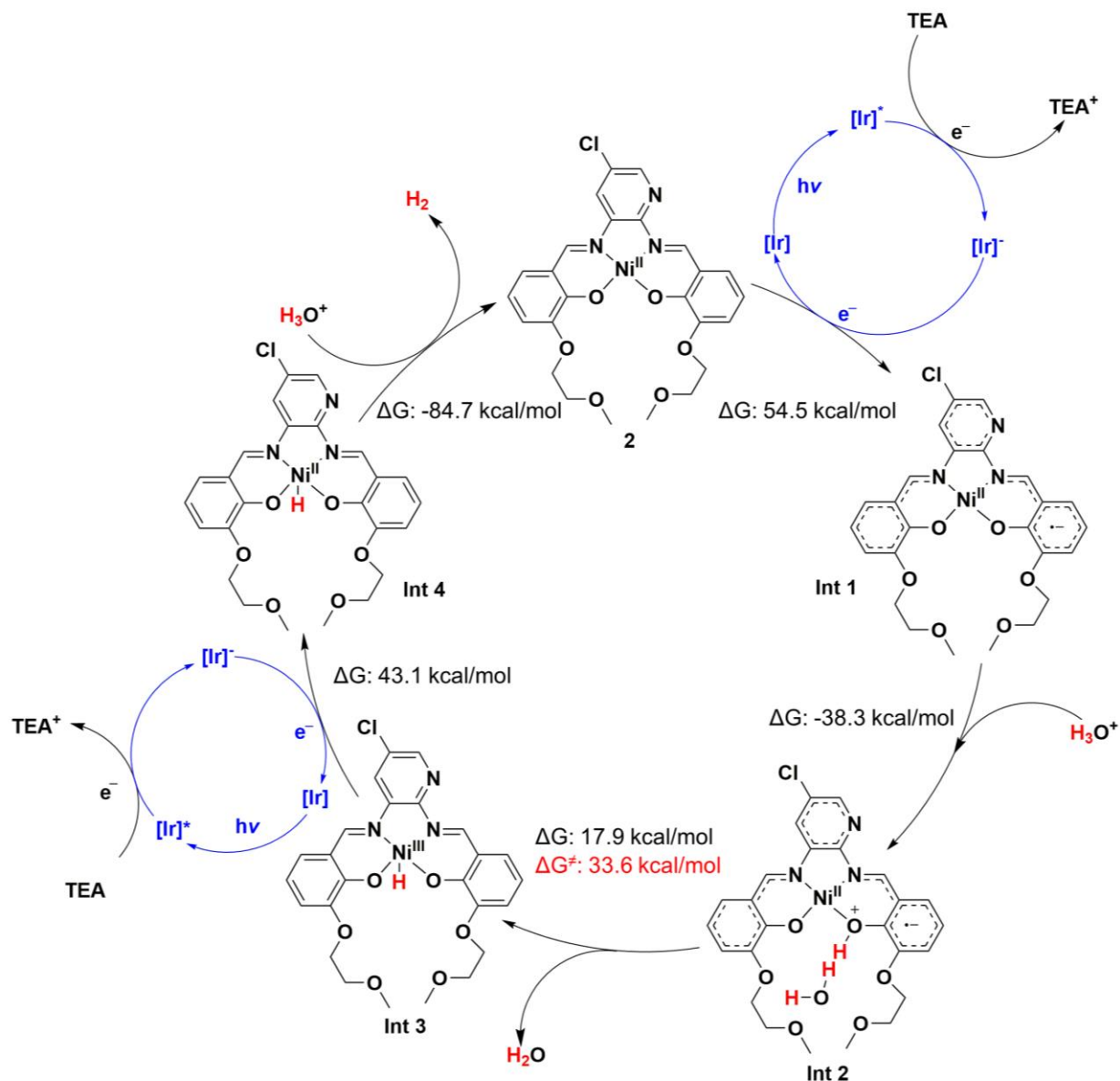
**Figure 6.** CV of 1.0 mM of **2** (red) and **3** (blue) in 0.10 M  $n\text{-Bu}_4\text{NPF}_6$  in THF with a glassy carbon electrode (3 mm diameter) at a scan rate of  $100 \text{ mV s}^{-1}$ . The CV of just the 0.10 M  $n\text{-Bu}_4\text{NPF}_6$  electrolyte solution in THF is the black line, confirming that THF is stable down to -3.0 V vs.  $\text{Fc}^+/\text{Fc}$ .

To elucidate the resting state of the **2** in the photocatalytic reaction, steady-state UV-visible spectroscopy was used to monitor the reaction over time. In the first 10 min of the reaction, the characteristic absorption of **2** at 380 nm decreases, while the weak absorption band from 580 – 700 nm, which is characteristic of the  $2^-$ , increases (Figure S16, SI). These changes become more prominent after 20 min of irradiation. A separate experiment was also carried out, starting with  $2^-$  instead of **2**, which showed a gradual recovery of the absorption band at 380 nm (Figure S16, SI). The spectra obtained in both conditions suggest that  $2^-$  is a likely resting state of **2** during the catalytic cycle under irradiation by visible light. With this in mind, further DFT calculations were carried out to map out a plausible reaction pathway and verify the impact of the pendant ether arms on the H<sub>2</sub> evolution by **2**.

DFT calculations were performed by using the M06 functional and the Def2-SVP basis set within the Gaussian 09 software. This combination of functional and basis set was found to provide a reasonable agreement with the experimentally observed physical parameters such as the experimental bond distances and angles of **2**, and also gave a reasonable calculated H<sub>2</sub> evolution route (Figure 7). Neutral H<sub>2</sub>O, which could have been a potential proton donor in this reaction, was first considered for the DFT calculations. However, the calculation showed that H<sub>2</sub>O was not capable of functioning as a proton donor since the O-H bond did not break with a reasonable barrier during the calculation. Instead, H<sub>3</sub>O<sup>+</sup> ions were found to provide a reasonable mechanism. To examine if an increase in pH could be another contributing reason for the decline in activity over prolonged irradiation because the concentration of H<sub>3</sub>O<sup>+</sup> ions would decrease over the course of the HER, we conducted experiments using a solution containing higher concentrations of TEA and introduced acetic acid as a buffer to around pH of 9.9. We observed that although the amount of H<sub>2</sub> evolved from the buffered solution was initially higher (Figure S17, SI), the H<sub>2</sub> production still

leveled off after 4 h of irradiation, similar to our original unbuffered solutions. The pH of the buffered solution before and after irradiation was also recorded, confirming that there was no significant variation in the pH when H<sub>2</sub> evolution had ceased. Therefore, we believe that the deactivation of **2** described above is still the main reason that the H<sub>2</sub> evolution halts in our photocatalytic system and not because of the depletion of H<sub>3</sub>O<sup>+</sup> ions over the course of the reaction.

We propose that **2** first undergoes an endothermic one-electron reduction by [Ir]<sup>-</sup> to form **2**<sup>-</sup> (**Int 1**), with the unpaired electron delocalized on the ligand with little Ni contribution. Subsequently, **Int 1** is protonated at one of the phenolic O atoms in an exergonic step (-38.3 kcal/mol) likely due to its largest spin density in the calculated highest occupied molecular orbital (HOMO). In the following step, a proton transfer from the phenolic O atom to Ni occurs to form **Int 3**, mediated by H<sub>2</sub>O as a proton shuttle with a kinetic barrier of 33.6 kcal/mol.<sup>36</sup> **Int 3** is then reduced by [Ir]<sup>-</sup> to give **Int 4**, and the Ni<sup>II</sup> hydride is readily protonated to release a molecule of H<sub>2</sub> and regenerate **2** in a highly exergonic process (-84.7 kcal/mol).



**ΔG<sup>‡</sup>:** Energy barrier of transition state.

**Figure 7.** Proposed pathway for H<sub>2</sub> evolution catalyzed by 2 based on DFT calculations of the energy levels of Ni-containing intermediates during the catalytic cycle. The thermodynamics in this cycle were obtained by including TEA as the sacrificial electron donor, whereas [Ir] (blue parts of the cycle) was not included in the DFT calculations since it served only as a photocatalyst.

In addition, we also specifically probed the role of H<sub>2</sub>O when it is cradled within the ether arms of **2**. The calculations show that H<sub>2</sub> evolution can only occur if a Ni hydride (**Int 4**) is formed, and the formation of the hydride **Int 3** required the presence of a H<sub>2</sub>O molecule near Ni to act as a proton shuttle from the phenolic O atom. Without this crucial Ni-H formation step, the second approach of H<sub>3</sub>O<sup>+</sup> only results in further protonation of another phenolic O atom, after which there is no energetically accessible route for H<sub>2</sub> formation (Figure 8). The encapsulation of water molecules by supramolecular systems such as benzo crown ethers and rotaxanes have been previously reported to influence the pK<sub>a</sub> and catalytic activity of the water,<sup>37</sup> lending support to our proposal that H<sub>3</sub>O<sup>+</sup> trapping by the ether arms of **2** played a vital role in our photocatalytic system. As such, the DFT calculations highlight the importance of the second coordination sphere ether functionality in hydrogen bonding to H<sub>2</sub>O as a proton shuttle to facilitate H<sub>2</sub> evolution. The full proposed mechanism is illustrated in Figure 7.

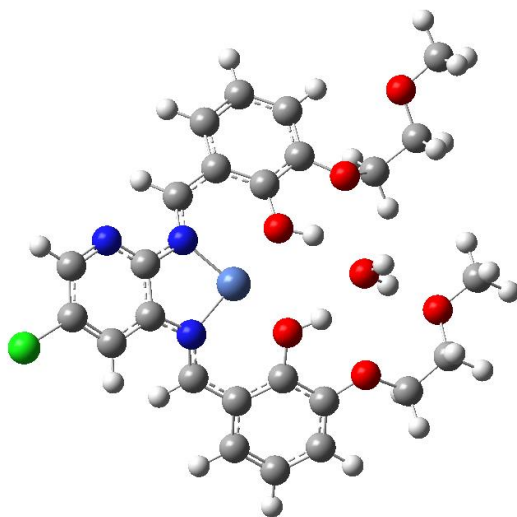


**Figure 8.** DFT calculations showing the double protonation on the ligand, which does not result in H<sub>2</sub> evolution.

## Conclusion

In summary, we have shown that **2** can operate as an efficient homogeneous catalyst for H<sub>2</sub> evolution with TONs up to 3880, which is among the best for molecular Ni complexes in molecular photocatalytic systems with neutral water as the proton source. Both steady-state and time-resolved optical spectroscopy combined with EPR spectroscopy provided insights into the initial elementary steps of the photocatalytic cycle involving a ligand-centered reduced intermediate. Moreover, DFT calculations supported a model where the second-sphere ether arms cradle H<sub>2</sub>O as a proton shuttle in close proximity to the Ni center and promotes a vital proton transfer between the phenolic O atom and the metal center. Our detailed spectroscopic and computational studies have allowed us to extract critical insights into a catalytic cycle that could be a potential solution for the storage and utilization of renewable energy. In addition, these results present a starting point for future developments of a broad class of H<sub>2</sub> evolution catalysts that employ alternative proton shuttles than amines in the second coordination sphere in artificial photosynthetic constructs driven by visible light in aqueous solutions.

## Experimental Section

**Materials and Methods** Deuterated solvents were purchased from Cambridge Isotope Laboratories. Chemicals were obtained from Sigma-Aldrich, Alfa-Aesar, and Tokyo Chemical Industry Co., Ltd. (TCI). Unless otherwise noted, the commercial reagents were used as purchased. Compound Ir<sup>III</sup>(ppy)<sub>2</sub>(dtbbpy) (ppy = 2-phenylpyridine; dtbbpy = 4,4'-di-*tert*-butyl-2,2'-bipyridine) was synthesized according to a previously published procedure.<sup>38</sup> The <sup>1</sup>H and <sup>13</sup>C spectra were recorded at room temperature on Bruker AVANCE 400 MHz and Bruker AV-300

(300 MHz) NMR spectrometers. The  $^1\text{H}$  and  $^{13}\text{C}$  chemical shifts ( $\delta$  reported in ppm) are referenced to the residual solvent signal(s). UV-visible spectroscopic measurements were performed using a Shimadzu UV-3600 UV-Vis-NIR spectrophotometer. Elemental analyses were performed with an Elementar vario MICRO cube analyser. High-resolution mass spectra (HR-MS) were obtained with a Q-TOF Premier LC HR mass spectrometer.

**Cyclic Voltammetry** The controlled-potential coulometric experiments were performed using a Biologic SP-300 potentiostat. A three-electrode electrochemical cell was used with a glassy carbon working electrode (3 mm in diameter from BASi®), a Pt wire counter electrode, and another Pt wire as a pseudoreference electrode. Ferrocene (2 equiv. of catalyst,  $E_{\text{Fc}^+/\text{Fc}}^0 = +0.64 \text{ V vs. NHE}$ )<sup>39</sup> was added as the internal standard in anhydrous ACN. Before each experiment, the working electrode (glassy carbon) was polished using a 0.05  $\mu\text{m}$  alumina suspension on a polishing pad, followed by sonication in deionized (DI) water for 10 min, and dried in air. The saturated Ar solutions were prepared by bubbling Ar through the solvents for 30 min.

**Scan Rate Dependence Study** In an electrochemical cell, 1.0 mM of **2** was dissolved in 0.10 M *n*-Bu<sub>4</sub>NPF<sub>6</sub> in ACN (5 mL). CV measurements were collected at various scan rates ranging from 100  $\text{mV s}^{-1}$  to 1000  $\text{mV s}^{-1}$ .

**Photocatalytic H<sub>2</sub> Evolution Experiment** The specific conditions, such as the reagent concentrations and reaction time intervals, have been summarized in Table S1. Typically, [Ir], **2**, and TEA (0.10 M) in 5.0 mL MeOH (5% H<sub>2</sub>O) were added to a 27 mL Schlenk tube together with a stir bar. The solution was deoxygenated by bubbling with Ar for 20 min after the Schlenk tube was sealed with a septum. The absence of O<sub>2</sub> in the Schlenk tube was verified by a GC (Agilent 7890A gas-chromatograph with a thermal conductivity detector, a 5 Å 2 mm  $\times$  5 m molecular sieve column, and Ar as the carrier gas) before irradiation. The tube was irradiated by visible light

supplied by a 300 W xenon lamp with a 420 nm-cutoff UV light filter. After the time intervals shown in Table S1, a gas sample (0.50 mL) was taken from the headspace of the Schlenk tube and analyzed by GC to determine the amount of generated H<sub>2</sub>.

**Preparation of TEA/acetic Acid Buffer** A buffer solution for the photocatalytic reaction was prepared by adding 0.10 mL of acetic acid, 20.0 mL of TEA, and 2.50 mL of DI water to 50.0 mL of methanol.

**Transient Absorption Measurements** The transient absorption and emission measurements were performed using an Edinburgh Instruments LP920 transient absorption spectrometer equipped with a pulsed Xe probe lamp in conjunction with a Nd:YAG laser (Continuum Surelite II-10) as the excitation source. The laser pulse width is 5-8 ns and the repetition rate is 10 Hz. During transient absorption measurements, the pulses are synchronized with the LP920 system at a frequency of 1 Hz. The pulse energy used was between 6-23 mJ/pulse.

The data were fit to single exponential or biexponential functions to obtain the time constants for the nanosecond transient optical spectroscopic signals according to the following equation:

$$y = y_0 + A_1 e^{-(t-\tau_0)/\tau_1}$$

The parameters  $y_0$ ,  $\tau_0$ ,  $A_n$ , and  $\tau_n$  were determined by a least-squares fitting procedure in Origin. The term  $y_0$  corresponds to the vertical intercept at long lifetimes where the signal decays to a ‘permanent’ absorption (positive  $y_0$ ) or bleach (negative  $y_0$ ). The variable  $\tau_0$  is the delay time of the excitation pulse from the start of the probe measurement during each photoexcitation cycle.  $A_l$  is the change in optical density after irradiation and  $\tau_l$  is the corresponding time constant.

**Stern-Volmer Plot for the Quenching of [Ir(ppy)<sub>2</sub>(dtbbpy)]<sup>3+</sup> by Triethylamine** As the concentration of TEA increases, the lifetime  $\tau$  of the signal owing to [Ir]<sup>3+</sup> decreases. The

bimolecular quenching rate constant,  $k_q$ , is related to the lifetime,  $\tau$  of  $[\text{Ir}]^{+*}$  in the presence of TEA with a concentration of  $[Q]$  by the Stern-Volmer equation:

$$\frac{\tau_0}{\tau} = 1 + k_q \tau_0 [Q]$$

where  $\tau_0$  is the lifetime of  $[\text{Ir}]^{+*}$  in the absence of TEA

The bimolecular rate constant,  $k_q$ , of the of  $[\text{Ir}]^{+*}$  by TEA can be obtained by plotting a graph of  $\tau_0/\tau$  against  $[Q]$  with a fixed vertical intercept of 1. The gradient ( $k_q \tau_0$ ) was determined to be  $2.22 \pm 0.07 \text{ M}^{-1}$  and  $\tau_0$  was determined to be  $3.90 \pm 0.20 \text{ } \mu\text{s}$ . This gives a rate constant,  $k_q$ , of  $5.66 \times 10^6 \text{ M}^{-1} \text{ s}^{-1}$ .

**Stern-Volmer Plot for the Quenching of  $[\text{Ir}(\text{ppy})_2(\text{dtbbpy})]^{+*}$  by **2**** As the concentration of **2** increases, the lifetime  $\tau$  of the signal owing to  $[\text{Ir}]^{+*}$  decreases. The quenching rate constant,  $k_q$ , is related to the lifetime,  $\tau$ , of  $[\text{Ir}]^{+*}$  in the presence of **2** with a concentration of  $[Q]$  by the Stern-Volmer equation:

$$\frac{\tau_0}{\tau} = 1 + k_q \tau_0 [Q]$$

where  $\tau_0$  is the lifetime of  $[\text{Ir}]^{+*}$  in the absence of **2** and can be obtained by plotting a graph of  $\tau_0/\tau$  against  $[Q]$  with a fixed vertical intercept of 1. This gives a rate constant,  $k_q$ , of  $3.56 \times 10^9 \text{ M}^{-1} \text{ s}^{-1}$ .

**TON calculation** The TON and TOF number of  $\text{H}_2$  generated from the photocatalytic experiments were calculated by the following equations:

$$\text{TON} = n_{\text{H}_2}/n_{\text{cat}} \text{ (mol H}_2 \text{ per mol catalyst)}$$

In the equation,  $n_{\text{H}_2}$  is the number of moles of  $\text{H}_2$  generated, and  $n_{\text{cat}}$  is the number of moles of catalyst used in the experiment.

**DFT calculation** All calculations were performed with the Gaussian 09 (Rev. E.01) program.<sup>40</sup> Geometry optimization was conducted by using the M06 functional.<sup>41</sup> The Def2-SVP basis set was employed for all atoms.<sup>42</sup> The vibrational analysis and thermodynamic information at 298.15 K were calculated with the keyword Freq in Gaussian. The PCM solvent model was used in the geometry optimizations for all calculations.

**EPR Measurements** The X-band EPR spectra were recorded on either a JEOL FA200 spectrometer or a Bruker ELEXSYS spectrometer. The EPR spectra were obtained at room temperature with the microwave frequency from 9200 to 9850 MHz. The spectrum for **2**<sup>•</sup> was obtained in the solid-state EPR at room temperature. The microwave frequency modulation amplitude was 0.006, time constant was 0.08192, power used was 2  $\mu$ W, and microwave frequency was at 9850 MHz. The EPR spectrum for sodium anthracenide was obtained as a solution in diethyl ether at room temperature. The microwave frequency was at 9200 MHz.

**Preparation of Solid-State Sample for EPR Measurement** The magnesium anthracene-THF complex (151 mg, 0.360 mmol) was added to **2** (200 mg, 0.360 mmol) in anhydrous THF and stirred at room temperature for 12 h. The solvent was removed under vacuum to obtain a dark green powder. The dark green residue was then washed with diethyl ether followed by pentane. The resulting solid was transferred to a J. Young EPR tube for the EPR experiment.

## ASSOCIATED CONTENT

### Supporting Information

The Supporting Information is available free of charge via the internet at <http://pubs.acs.org>. Synthetic details of the ligand and Ni complexes, spectroscopic characterization, essential crystallographic data and photocatalytic experimental results.

X-ray crystallographic data of **2** is deposited under CCDC 1849083 (CIF).

## AUTHOR INFORMATION

### Corresponding Authors

\* Email: [hansen@ntu.edu.sg](mailto:hansen@ntu.edu.sg); Tel: +65 65923182.

### Notes

The authors declare no competing financial interest.

## ACKNOWLEDGMENT

H.S.S. is supported by an NTU start-up grant (M4081012) and MOE Tier 1 grants (RG 12/16 and RG 13/17). The authors acknowledge the support from the Solar Fuels Laboratory at NTU. The authors also gratefully acknowledge the Agency for Science, Technology and Research (A\*STAR), AME IRG grants A1783c0002, A1783c0003, and A1783c0007 for funding this research. Y.L. thanks NTU for financial support *via* a MOE Tier 1 grant (RG 116/15). The authors also thank Professors Rong Xu and Mikinori Kuwata on advice regarding the detection of H<sub>2</sub> and D<sub>2</sub> by GC.

## REFERENCES

- (1) Barber, J., Photosynthetic Energy Conversion: Natural and Artificial. *Chem. Soc. Rev.* **2009**, 38, 185-196.
- (2) Han, Z.; Eisenberg, R., Fuel from Water: The Photochemical Generation of Hydrogen from Water. *Acc. Chem. Res.* **2014**, 47, 2537-2544.

- (3) (a) Chen, X.; Shen, S.; Guo, L.; Mao, S. S., Semiconductor-Based Photocatalytic Hydrogen Generation. *Chem. Rev.* **2010**, *110*, 6503-6570; (b) Sivula, K.; van de Krol, R., Semiconducting Materials for Photoelectrochemical Energy Conversion. *Nat. Rev. Mater.* **2016**, *1*, 15010; (c) Ran, J.; Zhang, J.; Yu, J.; Jaroniec, M.; Qiao, S. Z., Earth-Abundant Cocatalysts for Semiconductor-Based Photocatalytic Water Splitting. *Chem. Soc. Rev.* **2014**, *43*, 7787-7812; (d) Click, K. A.; Beauchamp, D. R.; Huang, Z.; Chen, W.; Wu, Y., Membrane-Inspired Acidically Stable Dye-Sensitized Photocathode for Solar Fuel Production. *J. Am. Chem. Soc.* **2016**, *138*, 1174-1179.
- (4) (a) Bard, A. J.; Fox, M. A., Artificial Photosynthesis: Solar Splitting of Water to Hydrogen and Oxygen. *Acc. Chem. Res.* **1995**, *28*, 141-145; (b) Sattler, W.; Ener, M. E.; Blakemore, J. D.; Rachford, A. A.; LaBeaume, P. J.; Thackeray, J. W.; Cameron, J. F.; Winkler, J. R.; Gray, H. B., Generation of Powerful Tungsten Reductants by Visible Light Excitation. *J. Am. Chem. Soc.* **2013**, *135*, 10614-10617.
- (5) (a) Esswein, A. J.; Nocera, D. G., Hydrogen Production by Molecular Photocatalysis. *Chem. Rev.* **2007**, *107*, 4022-4047; (b) Chang, C. J.; Chang, M. C.; Damrauer, N. H.; Nocera, D. G., Proton-Coupled Electron Transfer: A Unifying Mechanism for Biological Charge Transport, Amino Acid Radical Initiation and Propagation, and Bond Making/Breaking Reactions of Water and Oxygen. *Biochim. Biophys. Acta.* **2004**, *1655*, 13-28.
- (6) (a) Pfeffer, M. G.; Kowacs, T.; Wächtler, M.; Guthmüller, J.; Dietzek, B.; Vos, J. G.; Rau, S., Optimization of Hydrogen-Evolving Photochemical Molecular Devices. *Angew. Chem. Int. Ed.* **2015**, *54*, 6627-6631; (b) Ozawa, H.; Haga, M.-A.; Sakai, K., A Photo-Hydrogen-Evolving Molecular Device Driving Visible-Light-Induced EDTA-Reduction of Water into Molecular Hydrogen. *J. Am. Chem. Soc.* **2006**, *128*, 4926-4927.
- (7) (a) Cline, E. D.; Adamson, S. E.; Bernhard, S., Homogeneous Catalytic System for Photoinduced Hydrogen Production Utilizing Iridium and Rhodium Complexes. *Inorg. Chem.* **2008**, *47*, 10378-10388; (b) Xie, J.; Li, C.; Zhou, Q.; Wang, W.; Hou, Y.; Zhang, B.; Wang, X., Large Improvement in the Catalytic Activity due to Small Changes in the Diimine Ligands: New Mechanistic Insight into the Dirhodium (II, II) Complex-Based Photocatalytic H<sub>2</sub> Production. *Inorg. Chem.* **2012**, *51*, 6376-6384.
- (8) Pitman, C. L.; Miller, A. J., Molecular Photoelectrocatalysts for Visible Light-Driven Hydrogen Evolution from Neutral Water. *ACS Catal.* **2014**, *4*, 2727-2733.
- (9) Curtin, P. N.; Tinker, L. L.; Burgess, C. M.; Cline, E. D.; Bernhard, S., Structure– Activity Correlations Among Iridium (III) Photosensitizers in a Robust Water-Reducing System. *Inorg. Chem.* **2009**, *48*, 10498-10506.
- (10) (a) Du, P.; Eisenberg, R., Catalysts Made of Earth-Abundant Elements (Co, Ni, Fe) for Water Splitting: Recent Progress and Future Challenges. *Energy Environ. Sci.* **2012**, *5*, 6012-6021; (b) Koshiba, K.; Yamauchi, K.; Sakai, K., A Nickel Dithiolate Water Reduction Catalyst Providing Ligand-Based Proton-Coupled Electron-Transfer Pathways. *Angew. Chem. Int. Ed.* **2017**, *56*, 4247-4251; (c) Beyene, B. B.; Mane, S. B.; Hung, C. H., Highly Efficient Electrocatalytic Hydrogen Evolution from Neutral Aqueous Solution by a Water-Soluble Anionic Cobalt(II) Porphyrin. *Chem. Commun.* **2015**, *51*, 15067-15070.
- (11) (a) Fihri, A.; Artero, V.; Razavet, M.; Baffert, C.; Leibl, W.; Fontecave, M., Cobaloxime-Based Photocatalytic Devices for Hydrogen Production. *Angew. Chem., Int. Ed.* **2008**, *120*, 574-577; (b) Dempsey, J. L.; Brunschwig, B. S.; Winkler, J. R.; Gray, H. B., Hydrogen Evolution Catalyzed by Cobaloximes. *Acc. Chem. Res.* **2009**, *42*, 1995-2004; (c) McCormick, T. M.; Calitree, B. D.; Orchard, A.; Kraut, N. D.; Bright, F. V.; Detty, M. R.;

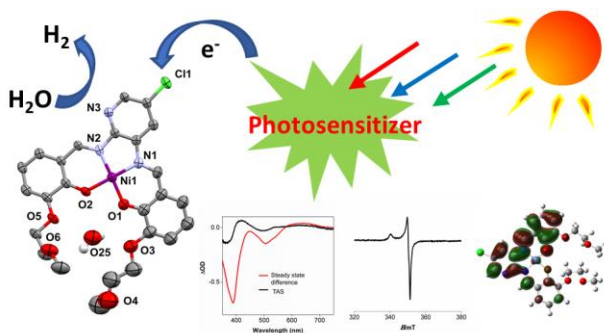
- Eisenberg, R., Reductive Side of Water Splitting in Artificial Photosynthesis: New Homogeneous Photosystems of Great Activity and Mechanistic Insight. *J. Am. Chem. Soc.* **2010**, *132*, 15480-15483; (d) Kaeffer, N.; Chavarot-Kerlidou, M.; Artero, V., Hydrogen Evolution Catalyzed by Cobalt Diimine–Dioxime Complexes. *Acc. Chem. Res.* **2015**, *48*, 1286-1295.
- (12) (a) Khnayzer, R. S.; Thoi, V. S.; Nippe, M.; King, A. E.; Jurss, J. W.; El Roz, K. A.; Long, J. R.; Chang, C. J.; Castellano, F. N., Towards a Comprehensive Understanding of Visible-Light Photogeneration of Hydrogen from Water using Cobalt(II) Polypyridyl Catalysts. *Energy Environ. Sci.* **2014**, *7*, 1477-1488; (b) Nippe, M.; Khnayzer, R. S.; Panetier, J. A.; Zee, D. Z.; Olaiya, B. S.; Head-Gordon, M.; Chang, C. J.; Castellano, F. N.; Long, J. R., Catalytic Proton Reduction with Transition Metal Complexes of the Redox-Active Ligand Bpy2PYMe. *Chem. Sci.* **2013**, *4*, 3934-3945.
- (13) (a) Helm, M. L.; Stewart, M. P.; Bullock, R. M.; DuBois, M. R.; DuBois, D. L., A Synthetic Nickel Electrocatalyst with a Turnover Frequency Above 100,000 s<sup>-1</sup> for H<sub>2</sub> Production. *Science* **2011**, *333*, 863-866; (b) Jacobsen, G. M.; Yang, J. Y.; Twamley, B.; Wilson, A. D.; Bullock, R. M.; DuBois, M. R.; DuBois, D. L., Hydrogen Production Using Cobalt-Based Molecular Catalysts Containing a Proton Relay in the Second Coordination Sphere. *Energy Environ. Sci.* **2008**, *1*, 167-174; (c) Rakowski, M.; DuBois, D. L., Development of Molecular Electrocatalysts for CO<sub>2</sub> Reduction and H<sub>2</sub> Production/Oxidation. *Acc. Chem. Res.* **2009**, *42*, 1974-1982.
- (14) McLaughlin, M. P.; McCormick, T. M.; Eisenberg, R.; Holland, P. L., A Stable Molecular Nickel Catalyst for the Homogeneous Photogeneration of Hydrogen in Aqueous Solution. *Chem. Commun.* **2011**, *47*, 7989-7991.
- (15) Gross, M. A.; Reynal, A.; Durrant, J. R.; Reisner, E., Versatile Photocatalytic Systems for H<sub>2</sub> Generation in Water Based on an Efficient DuBois-Type Nickel Catalyst. *J. Am. Chem. Soc.* **2014**, *136*, 356-366.
- (16) (a) McNamara, W. R.; Han, Z.; Alperin, P. J.; Brennessel, W. W.; Holland, P. L.; Eisenberg, R., A Cobalt–Dithiolene Complex for the Photocatalytic and Electrocatalytic Reduction of Protons. *J. Am. Chem. Soc.* **2011**, *133*, 15368-15371; (b) McNamara, W. R.; Han, Z.; Yin, C.-J. M.; Brennessel, W. W.; Holland, P. L.; Eisenberg, R., Cobalt-Dithiolene Complexes for the Photocatalytic and Electrocatalytic Reduction of Protons in Aqueous Solutions. *Proc. Natl. Acad. Sci. U.S.A.* **2012**, *109*, 15594-15599.
- (17) (a) Han, Z.; McNamara, W. R.; Eum, M. S.; Holland, P. L.; Eisenberg, R., A Nickel Thiolate Catalyst for the Long-Lived Photocatalytic Production of Hydrogen in a Noble-Metal-Free System. *Angew. Chem. Int. Ed.* **2012**, *51*, 1667-1670; (b) Han, Z.; Shen, L.; Brennessel, W. W.; Holland, P. L.; Eisenberg, R., Nickel Pyridinethiolate Complexes as Catalysts for the Light-Driven Production of Hydrogen from Aqueous Solutions in Noble-Metal-Free Systems. *J. Am. Chem. Soc.* **2013**, *135*, 14659-14669.
- (18) (a) Lee, C. H.; Dogutan, D. K.; Nocera, D. G., Hydrogen Generation by Hangman Metalloporphyrins. *J. Am. Chem. Soc.* **2011**, *133*, 8775-8777; (b) Graham, D. J.; Nocera, D. G., Electrocatalytic H<sub>2</sub> Evolution by Proton-Gated Hangman Iron Porphyrins. *Organometallics* **2014**.
- (19) Dokic, M.; Soo, H. S., Artificial Photosynthesis by Light Absorption, Charge Separation, and Multielectron Catalysis. *Chem. Commun.* **2018**, *54*, 6554-6572.
- (20) (a) Soo, H. S.; Macnaughtan, M. L.; Weare, W. W.; Yano, J.; Frei, H. M., EXAFS Spectroscopic Analysis of Heterobinuclear TiOMn Charge-Transfer Chromophore in

- Mesoporous Silica. *J. Phys. Chem. C* **2011**, *115*, 24893-24905; (b) Kee, J. W.; Ng, Y. Y.; Kulkarni, S. A.; Xu, K.; Ganguly, R.; Lu, Y.; Hirao, H.; Soo, H. S., Development of Bis(arylimino)acenaphthene (BIAN) Copper Complexes as Visible Light Harvesters for Potential Photovoltaic Applications. *Inorg. Chem. Front.* **2016**, 651-662.
- (21) Muduli, S. K.; Wang, S.; Chen, S.; Ng, C. F.; Huan, C. H. A.; Sum, T. C.; Soo, H. S., Mesoporous Cerium Oxide Nanospheres for the Visible-Light Driven Photocatalytic Degradation of Dyes. *Beilstein J. Nanotechnol.* **2014**, *5*, 517-523.
- (22) (a) Shao, H.; Muduli, S. K.; Tran, P. D.; Soo, H. S., Enhancing Electrocatalytic Hydrogen Evolution by Nickel Salicylaldimine Complexes with Alkali Metal Cations in Aqueous Media. *Chem. Commun.* **2016**, *52*, 2948-2951; (b) Gazi, S.; Hung Ng, W. K.; Ganguly, R.; Putra Moeljadi, A. M.; Hirao, H.; Soo, H. S., Selective Photocatalytic C-C Bond Cleavage under Ambient Conditions with Earth Abundant Vanadium Complexes. *Chem. Sci.* **2015**, *6*, 7130-7142; (c) Lim, J. H.; Engelmann, X.; Corby, S.; Ganguly, R.; Ray, K.; Soo, H. S., C-H Activation and Nucleophilic Substitution in a Photochemically Generated High Valent Iron Complex. *Chem. Sci.* **2018**, *9*, 3992-4002; (d) Ghosh, D.; Febriansyah, B.; Gupta, D.; Ng, L. K.; Xi, S.; Du, Y.; Baikie, T.; Dong, Z.; Soo, H. S., Hybrid Nanomaterials with Single-Site Catalysts by Spatially Controllable Immobilization of Nickel Complexes via Photoclick Chemistry for Alkene Epoxidation. *ACS Nano* **2018**; (e) Das, S. P.; Ganguly, R.; Li, Y.; Soo, H. S., Nucleophilic Reactivity and Electrocatalytic Reduction of Halogenated Organic Compounds by Nickel o-Phenylenedioxamidate Complexes. *Dalton Trans.* **2016**, *45*, 13556-13564; (f) Gazi, S.; Đokić, M.; Moeljadi, A. M. P.; Ganguly, R.; Hirao, H.; Soo, H. S., Kinetics and DFT Studies of Photoredox Carbon–Carbon Bond Cleavage Reactions by Molecular Vanadium Catalysts under Ambient Conditions. *ACS Catal.* **2017**, *7*, 4682-4691.
- (23) (a) Kumar, A.; Lionetti, D.; Day, V. W.; Blakemore, J. D., Trivalent Lewis Acidic Cations Govern the Electronic Properties and Stability of Heterobimetallic Complexes of Nickel. *Chem. Eur. J.* **2018**, *24*, 141-149; (b) Van Staveren, C. J.; Van Eerden, J.; Van Veggel, F. C. J. M.; Harkema, S.; Reinhoudt, D. N., Cocomplexation of Neutral Guests and Electrophilic Metal Cations in Synthetic Macrocyclic Hosts. *J. Am. Chem. Soc.* **1988**, *110*, 4994-5008; (c) Reath, A. H.; Ziller, J. W.; Tsay, C.; Ryan, A. J.; Yang, J. Y., Redox Potential and Electronic Structure Effects of Proximal Nonredox Active Cations in Cobalt Schiff Base Complexes. *Inorg. Chem.* **2017**, *56*, 3713-3718.
- (24) (a) Chang, C. T.; Chen, C. L.; Liu, Y. H.; Peng, S. M.; Chou, P. T.; Liu, S. T., Coordination of Fluoro Ligands Toward Sodium Ions Makes the Difference: Aqua Sodium Ions Act as Bronsted Acids in Polymerization of Vinyl Ethers and Styrenes. *Inorg. Chem.* **2006**, *45*, 7590-2; (b) Cacciapaglia, R.; Mandolini, L., Catalysis by Metal Ions in Reactions of Crown Ether Substrates. *Chem. Soc. Rev.* **1993**, *22*, 221-231.
- (25) (a) McNamara, W. R.; Han, Z.; Alperin, P. J.; Brennessel, W. W.; Holland, P. L.; Eisenberg, R., A Cobalt–Dithiolene Complex for the Photocatalytic and Electrocatalytic Reduction of Protons. *J. Am. Chem. Soc.* **2011**, *133*, 15368-15371; (b) Suneesh, C. V.; Balan, B.; Ozawa, H.; Nakamura, Y.; Katayama, T.; Muramatsu, M.; Nagasawa, Y.; Miyasaka, H.; Sakai, K., Mechanistic Studies of Photoinduced Intramolecular and Intermolecular Electron Transfer Processes in RuPt-centred Photo-Hydrogen-Evolving Molecular Devices. *Phys. Chem. Chem. Phys.* **2014**, *16*, 1607-16.
- (26) Isse, A. A.; Gennaro, A.; Vianello, E., A Study of the Electrochemical Reduction Mechanism of Ni(Salophen) in DMF *Electrochim. Acta* **1992**, *37*, 113-118.

- (27) Costentin, C.; Passard, G.; Robert, M.; Saveant, J. M., Pendant Acid-base Groups in Molecular Catalysts: H-bond Promoters or Proton Relays? Mechanisms of the Conversion of CO<sub>2</sub> to CO by Electrogenenerated Iron(0) Porphyrins Bearing Prepositioned Phenol Functionalities. *J. Am. Chem. Soc.* **2014**, *136*, 11821-9.
- (28) (a) Lv, H.; Guo, W.; Wu, K.; Chen, Z.; Bacsa, J.; Musaev, D. G.; Geletii, Y. V.; Lauinger, S. M.; Lian, T.; Hill, C. L., A Noble-Metal-Free, Tetra-Nickel Polyoxotungstate Catalyst for Efficient Photocatalytic Hydrogen Evolution. *J. Am. Chem. Soc.* **2014**, *136*, 14015-14018; (b) Prier, C. K.; Rankic, D. A.; MacMillan, D. W. C., Visible Light Photoredox Catalysis with Transition Metal Complexes: Applications in Organic Synthesis. *Chem. Rev.* **2013**, *113*, 5322-5363.
- (29) Cozzi, P. G., Metal–Salen Schiff base complexes in catalysis: practical aspects. *Chem. Soc. Rev.* **2004**, *33*, 410-421.
- (30) (a) Zhang, W.; Wang, Y.; Wang, Z.; Zhong, Z.; Xu, R., Highly Efficient and Noble Metal-Free NiS/CdS Photocatalysts for H<sub>2</sub> Evolution from Lactic Acid Sacrificial Solution Under Visible Light. *Chem. Commun.* **2010**, *46*, 7631-3; (b) Gartner, F.; Sundararaju, B.; Surkus, A. E.; Boddien, A.; Loges, B.; Junge, H.; Dixneuf, P. H.; Beller, M., Light-Driven Hydrogen Generation: Efficient Iron-Based Water Reduction Catalysts. *Angew. Chem. Int. Ed.* **2009**, *48*, 9962-5; (c) Thermal conductivity/E<sup>-4</sup> W/mK (Fa. Messer, Switzerland): H<sub>2</sub> (1861) > He (1500) > D<sub>2</sub> (1310).
- (31) Cao, S. W.; Liu, X. F.; Yuan, Y. P.; Zhang, Z. Y.; Fang, J.; Loo, S. C.; Barber, J.; Sum, T. C.; Xue, C., Artificial Photosynthetic Hydrogen Evolution Over g-C<sub>3</sub>N<sub>4</sub> Nanosheets Coupled with Cobaloxime. *Phys. Chem. Chem. Phys.* **2013**, *15*, 18363-18366.
- (32) (a) Chen, L.; Chen, G.; Leung, C.-F.; Yiu, S.-M.; Ko, C.-C.; Anxolabéhère-Mallart, E.; Robert, M.; Lau, T.-C., Dual Homogeneous and Heterogeneous Pathways in Photo- and Electrocatalytic Hydrogen Evolution with Nickel (II) Catalysts Bearing Tetradentate Macrocyclic Ligands. *ACS Catal.* **2014**, *5*, 356-364; (b) Wang, C.; Cao, S.; Fu, W. F., A Stable Dual-Functional System of Visible-Light-Driven Ni(II) Reduction to a Nickel Nanoparticle Catalyst and Robust in situ Hydrogen Production. *Chem. Commun.* **2013**, *49*, 11251-11253; (c) Yamada, Y.; Miyahigashi, T.; Kotani, H.; Ohkubo, K.; Fukuzumi, S., Photocatalytic Hydrogen Evolution with Ni Nanoparticles by Using 2-phenyl-4-(1-naphthyl)quinolinium Ion as a Photocatalyst. *Energy Environ. Sci.* **2012**, *5*, 6111-6118.
- (33) (a) Bogdanovic, B., Magnesium Anthracene Systems and Their Application in Synthesis and Catalysis. *Acc. Chem. Res.* **1988**, *21*, 261-267; (b) Bogdanovic, B.; Janke, N.; Kinzelmann, H.-G., Use of Magnesium Anthracene.3 THF in Synthesis: Generation of Grignard Compounds and Other Reactions with Organic Halides. *Chem. Ber.* **1990**, 1507-1515.
- (34) Azevedo, F.; Freire, C.; de Castro, B., Reductive Electrochemical Study of Ni(II) Complexes with N<sub>2</sub>O<sub>2</sub> Schiff Base Complexes and Spectroscopic Characterisation of the Reduced Species. Reactivity towards CO. *Polyhedron* **2002**, *21*, 1695-1705.
- (35) Solis, B. H.; Maher, A. G.; Dogutan, D. K.; Nocera, D. G.; Hammes-Schiffer, S., Nickel Phlorin Intermediate Formed by Proton-Coupled Electron Transfer in Hydrogen Evolution Mechanism. *Proc. Natl. Acad. Sci. U.S.A* **2016**, *113*, 485-492.
- (36) Das, A.; Jha, A.; Gera, R.; Dasgupta, J., Photoinduced Charge Transfer State Probes the Dynamic Water Interaction with Metal–Organic Nanocages. *J. Phys. Chem. C* **2015**, *119*, 21234-21242.
- (37) (a) Costes, J.-P.; Dahan, F.; Laurent, J.-P., A Monomeric, Self-Assembling, Alkali-Metal Binding Nickel Complex: Reappraisal of the Original Model from Solid-State and Solution

- Studies. *Inorg. Chem.* **1994**, *33*, 2738-2742; (b) Kusaka, R.; Inokuchi, Y.; Ebata, T., Structure of Hydrated Clusters of Dibenzo-18-crown-6-ether in a Supersonic Jet--Encapsulation of Water Molecules in the Crown Cavity. *Phys. Chem. Chem. Phys.* **2008**, *10*, 6238-44; (c) Ragazzon, G.; Schafer, C.; Franchi, P.; Silvi, S.; Colasson, B.; Lucarini, M.; Credi, A., Remote Electrochemical Modulation of  $pK_a$  in a Rotaxane by Co-conformational Allostery. *Proc. Natl. Acad. Sci. U.S.A* **2018**, *115*, 9385-9390.
- (38) Querard, P.; Perepichka, I.; Zysman-Colman, E.; Li, C. J., Copper-Catalyzed Asymmetric sp(3) C-H Arylation of Tetrahydroisoquinoline Mediated by a Visible Light Photoredox Catalyst. *Beilstein J. Org. Chem.* **2016**, *12*, 2636-2643.
- (39) Thoi, V. S.; Sun, Y.; Long, J. R.; Chang, C. J., Complexes of Earth-Abundant Metals for Catalytic Electrochemical Hydrogen Generation under Aqueous Conditions. *Chem. Soc. Rev.* **2013**, *42*, 2388-2400.
- (40) *Gaussian 09, Revision E.01*, M. J. Frisch, G. W. T., H. B. Schlegel, G. E. Scuseria, M. A. Robb, J. R. Cheeseman, G. Scalmani, V. Barone, G. A. Petersson, H. Nakatsuji, X. Li, M. Caricato, A. Marenich, J. Bloino, B. G. Janesko, R. Gomperts, B. Mennucci, H. P. Hratchian, J. V. Ortiz, A. F. Izmaylov, J. L. Sonnenberg, D. Williams-Young, F. Ding, F. Lipparini, F. Egidi, J. Goings, B. Peng, A. Petrone, T. Henderson, D. Ranasinghe, V. G. Zakrzewski, J. Gao, N. Rega, G. Zheng, W. Liang, M. Hada, M. Ehara, K. Toyota, R. Fukuda, J. Hasegawa, M. Ishida, T. Nakajima, Y. Honda, O. Kitao, H. Nakai, T. Vreven, K. Throssell, J. A. Montgomery, Jr., J. E. Peralta, F. Ogliaro, M. Bearpark, J. J. Heyd, E. Brothers, K. N. Kudin, V. N. Staroverov, T. Keith, R. Kobayashi, J. Normand, K. Raghavachari, A. Rendell, J. C. Burant, S. S. Iyengar, J. Tomasi, M. Cossi, J. M. Millam, M. Klene, C. Adamo, R. Cammi, J. W. Ochterski, R. L. Martin, K. Morokuma, O. Farkas, J. B. Foresman, and D. J. Fox, Gaussian, Inc., Wallingford CT, **2016**.
- (41) Zhao, Y.; Truhlar, D. G., The M06 Suite of Density Functionals for Main Group Thermochemistry, Thermochemical Kinetics, Noncovalent Interactions, Excited States, and Transition Elements: Two New Functionals and Systematic Testing of Four M06-Class Functionals and 12 other Functionals. *Theor. Chem. Acc.* **2007**, *120*, 215-241.
- (42) Weigend, F.; Ahlrichs, R., Balanced Basis Sets of Split Valence, Triple Zeta Valence and Quadruple Zeta Valence Quality for H to Rn: Design and Assessment of Accuracy. *Phys. Chem. Chem. Phys.* **2005**, *7*, 3297-3305.

## Table of Contents graphic



A molecular Ni catalyst, comprising earth-abundant elements, for H<sub>2</sub> evolution from aqueous solutions driven by visible light is reported. Under optimized conditions, we observe a turnover number of up to 3880. Through nanosecond transient absorption, electron paramagnetic resonance, and UV-visible spectroscopic measurements, supported by density functional theory calculations, we demonstrate the involvement of ligand redox noninnocence and an ether-based, second coordination sphere, proton relay during the catalysis.